J. COMBIN. MATH. COMBIN. COMPUT. 127b (2025) 9219--9238

Journal of Combinatorial Mathematics
and Combinatorial Computing
www.combinatorialpress.com/jcmcc

Combinatorial Press

Parameter optimization of cataract IOL calculation model based on genetic algorithm and improvement of remote diagnosis and treatment effect

Hongxu Sun[1], Huan Liu[1], Wang Xi[1], Shouxi Lan[1], Xiaofei Dong[1, ✉]

[1] *Department of Ophthalmology, 967 Hospital of PLA Joint Logistic Support Force, Dalian, Liaoning, 116011, China*

ABSTRACT
Cataract, as an extremely common visual impairment disease, seriously affects the normal work and life of patients, and the optimization of cataract IOL model is of extraordinary significance to the diagnosis and treatment effect. The article collects ocular biological measurements of cataract surgery patients as experimental data, explores the radial basis function (RBF) neural network belonging to the field of artificial intelligence in the process of IOL calculation, and then introduces genetic algorithms to optimize the RBF neural network, and constructs the cataract IOL calculation model based on GA-RBF. The experimental results show that after combining the improved cataract IOL calculation model for telemedicine, the patient's hospitalization days were shortened by 3.06 d, and the hospitalization cost decreased by $1,383.7, meanwhile, the patient's satisfaction increased by 4.69%.

Keywords: IOL computational model, GA-RBF neural network, cataract, genetic algorithm, telepractice

1. Introduction

Cataract is an eye disease in which the cornea or lens of the eye becomes cloudy, resulting in poor vision. It is one of the most common ophthalmic diseases in the world and can seriously affect patients' daily life and work. The causes of cataract are many, including age, genetics, environmental factors, and ocular diseases [1-4]. With age, the proteins in the lens will degenerate and coagulate, causing the lens to become cloudy, which in turn affects the transmission and scattering of light, making the patient's vision blurred [5-6]. Cataract surgery is one of the effective methods for treating cataract, while IOL calculation refers to the selection of an appropriate IOL for the patient during cataract surgery in order to restore the patient's vision [7-9].

The aim of the surgery is to remove the cloudy lens and implant an IOL to restore the patient's vision. Before the surgery, the surgeon needs to perform a series of examinations on the patient, including

✉ Corresponding author.
E-mail address: yhhxxshx@163.com (X. Dong).
Received 01 March 2024; Revised 25 May 2024; Accepted 10 November 2024; Published Online 16 April 2025.
DOI: 10.61091/jcmcc127b-505

intraocular pressure measurement, fundus examination, corneal curvature measurement, etc., in order to determine the specific method of the surgery and the selection of the IOL [10-13]. IOL calculation is a crucial step in cataract surgery, and its purpose is to select the appropriate IOL to achieve the effect that the patient can see and recognize the objects better after the surgery. With the rapid development of science and technology, the application of telemedicine services is becoming more and more widespread [14-17]. Telemedicine service refers to the sharing of medical resources and the remote provision of medical services through the Internet, mobile communication and other technical means, which has an important role in the field of diagnosis and treatment of cataract [18-20].

The article first used a retrospective study by applying IOL Master 700 to collect ocular biological measurements of patients who underwent preoperative cataract surgery in the cataract department of an ophthalmology center, and the study subjects in the acquired clinical data were 50 adults with a total of 100 eyes (25 males and 25 females). Then, the RBF neural network was tuned in order to meet the requirements of predicting the ELP, and the RBF neural network was trained using training samples, and the weights ωi of the radial basis function neural network and the center width vector of the Gaussian basis function σi were optimized by the improved genetic algorithm (GA), and the new IOL formula GA-RBF was finally constructed.Subsequently, a new IOL formula GA-RBF was established based on the pre-operative ocular biometric measurements of the cataract patients acquired through the preoperative eye biological characteristic parameters collected from cataract patients before surgery, the near-axis schematic eye models of adults in three different age groups, namely, 21-40 years old, 41-60 years old, and 61-90 years old, were established based on the cataract clinical data. The model was compared with the Lion-Brennan eye model and the Navarro eye model, and the visual quality was evaluated. The accuracy of the calculation formula of IOL was also compared. Finally, cataract patients were selected as research subjects and treated in groups according to different modalities, and the clinical data were compared and analyzed to verify the validity of the methods in this paper.

2. Optimization of parameters of cataract IOL calculation model based on genetic algorithm

2.1. Information

2.1.1. General information. A retrospective study was used to collect data for statistical analysis of ocular biometric measurements of preoperative cataract patients at the Eye Center of the Second Hospital of Jilin University from November 2021 to December 2023, and the patients' ages ranged from 36 to 85 years old, with a total of 10,566 eyes, and the mean age was 66 (58-71) years old, and the study protocol was in accordance with the Declaration of Helsinki, and was approved by the Second Hospital of Jilin University's Ethics Committee for approval.

2.1.2. Inspection. All patients underwent routine pre-cataract examination and IOL master 700 to measure and record axial length, anterior chamber depth, lens thickness, corneal refractive power, aqueous humor depth, central corneal thickness, white to white, pupil diameter, corneal refractive power (including anterior surface refractive power K1K2, corneal full surface refractive power TK1/TK2, posterior corneal surface refractive power PK1/PK2), corneal astigmatism = K2-K1 (K1 and K2 are planar axis corneal refractive power, Steep axis corneal refractive power) and corneal astigmatism axis (Conventional astigmatism (WTR): the steepest meridian of the cornea is within 90±30 degrees, Reverse Gauge (ATR): the steepest meridian of the cornea is within 180±30 degrees, and oblique axis astigmatism: the steepest meridian is within 30~60 degrees or 120~150 degrees).

2.1.3. Inclusion and exclusion criteria:

1) Inclusion criteria

a. Patients preformed cataract surgery

b. Patients ⩾36 years old

2) Exclusion Criteria

a. Patients who cannot cooperate with IOL Master 700 measurement. b. Corneal lesions: corneal inflammation, trauma, and other diseases that affect corneal thickness and corneal refractive power measurement. c. Vitreous diseases: lesions with vitreous blood accumulation that affects the measurement and observation. d. Hemorrhagic diseases of the retina: central vein obstruction, branch vein obstruction, and so on. e. Retinal detachment. f. Trauma to the eye. g. Various kinds of surgical history that affects the ocular history of surgeries such as: post vitrectomy, excimer laser in situ keratomileusis, radial keratotomy, excimer laser keratomileusis, post IOL implantation, aphakia, corneal transplantation, retinal detachment, and other surgical cases. h: Patients with severe systemic diseases.

2.2. Constructing an IOL calculation formula

2.2.1. Determining the basic components of the IOL formula. The optical theories on which the current mainstream IOL refractive power calculation formulas are based are divided into two categories: one is based on classical Gaussian optics, which is characterized by the consideration of only proximal-axis light rays, which simplifies the calculation process and introduces the concept of the effective IOL position (ELP), i.e., the distance from the main corneal image-square plane to the main IOL image-square plane [21]. This parameter cannot be measured preoperatively, so the difference between the various formulas based on this theory is mainly in the prediction of the ELP. The other type of ray-tracing formulas, which strictly follow Snell's law, are characterized by the inclusion of non-proximal-axis rays, and their main prediction is the actual position of the IOL after surgery.

Assuming n is the refractive index of the aqueous humor, AL is the ocular axis in meters, m), K is the corneal curvature in diopters, D), Rx is the number of degrees of reserved refractive error in diopters, D), and V is the lens-eye distance in meters, m), the total refractive power provided by the spectacles, the cornea, and the IOL at the effective IOL position (ELP) can be calculated by the formula:

$$\frac{n}{AL-ELP} \tag{1}$$

The sum of the refractive power provided by the cornea and spectacles in the corneal plane, discussed separately, can be obtained by the following formula:

$$K+\frac{1}{\frac{1}{R_x}-V} \tag{2}$$

The refractive power provided by the cornea and spectacles on the ELP can be further calculated from equations (1) and (2):

$$\frac{n}{\frac{n}{K+\frac{1}{\frac{1}{Rx}-V}}-ELP} \tag{3}$$

Therefore, the refractive power P required to be supplied by the IOL in the ELP position can be calculated by the difference between Equation (1) and Equation (3):

$$P = \frac{n}{AL - ELP} - \frac{n}{\frac{n}{K + \frac{1}{\frac{1}{Rx} - V}} - ELP} \tag{4}$$

The refractive index of the aqueous humor $n = 1.336$, the distance between the lens eyes is usually taken as 12 mm, the eye axis and corneal curvature can be obtained by measurement before the operation, and the number of reserved refractive errors is determined by the ophthalmologists after communicating with the patients, so we only need to predict the value of the ELP in order to find out the refractive power provided by the required IOL.

When there is no reserved refractive error $(Rx = 0)$, there is no need to consider the refractive power provided by spectacles in the plane of the ELP, and the refractive power provided by the required IOL $P_{emmetropia}$ can be expressed as follows:

$$P_{emmetropia} = \frac{n}{AL - ELP} - \frac{n}{\frac{n}{K} - ELP} \tag{5}$$

2.2.2. Constructing training samples. Due to the limitations of current biometric techniques, the routine clinical measurements are the ocular axis (AL), corneal flat-axis curvature (K1), corneal steep-axis curvature (K2), and preoperative anterior chamber depth (ACD). For corneal curvature, it is routine to take the arithmetic mean (K) of the steep and flat corneal curvatures. For different IOLs, the A-constant can represent their characteristics to a certain extent, and here we chose to use the A-constant data provided in the optimization database of the European Collaboration for Laser Interferometry Biometry (ULIB) [22]. Although the use of ACD can increase the prediction accuracy, we do not consider ACD as one of the parameters for predicting IOLs for the time being, because the role of ACD in the currently commonly used IOL calculation formulas is not as large as that of the eye axis and corneal curvature, and because the increase in the number of parameters will result in the huge amount of samples required for training the AI.

Therefore, each set of data in the training samples should consist of the eye axis, mean corneal curvature, and IOL A constant, and we set the unit of eye axis as millimeter, and the unit of mean corneal curvature as refractive error.

The corresponding eye axis generates an isotropic series with 17.00 as the first term, 35.80 as the last term, and a tolerance of 0.4. The corresponding mean corneal curvature generates an isotropic series with 30.00 as the first term, 60.00 as the last term, and a tolerance of 0.5. Corresponding to the A constant generates an isotropic series with 114.00 as the first term, 123.00 as the last term, and a tolerance of 0.6. Arrange and combine the terms in the 3 sets of series in the form of (AL,K,A) to obtain all the data sets to be calculated.

It has been shown that the EVO formula has high accuracy at short eye axes, the Kane formula at normal eye axes, and the Barrett Universal II formula at long eye axes. Data with AL < 22.5 mm were entered into the EVO formula, data with 22.5 mm ⩽ AL ⩽ 25.5 mm were entered into the Kane formula, and data with AL > 25.5 mm were entered into the Barrett Universal II formula, which uniformly does not reserve spherical lens power, discards data outside the range of calculation of the formula, and records the formula-recommended IOL power (P) and the predicted remaining spherical lens degrees (Rx). The remaining data are sequentially substituted into the formula to invert the ELP, discard the data that are not solvable for the ELP in the real number range, and form the remaining data into a training sample.

2.2.3. GA optimized RBF neural network. In this paper, two parameters of GA optimized RBF neural network, namely, the weights between the implied layer and the output layer ω_i and the center width vector of Gaussian basis function σ_i, are optimized to improve the efficiency and training accuracy of the neural network, so as to improve the accurate prediction of the trend of the dosage change. When the value of population fitness meets the requirements of evolutionary accuracy or the genetic algorithm reaches the upper convergence limit of evolutionary iterations, the weights between the implied layer and the output layer ω_i and the Gaussian basis function center width vector σ_i are output after genetic optimization, and mapping conversion is performed to update the structure and parameters of the RBF neural network, and the improved optimization flow of the GA algorithm is shown in Fig. 1.

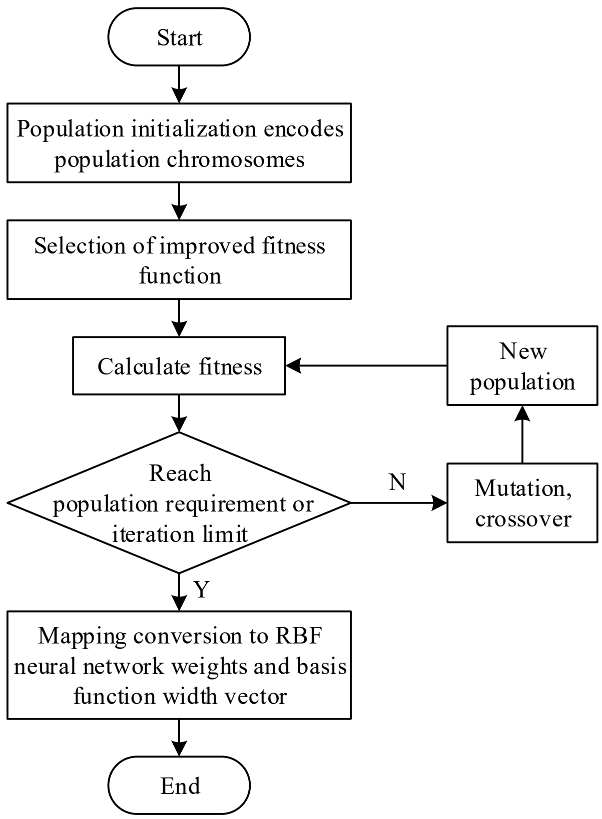

Fig. 1. Improve GA algorithm optimization process

The main optimization steps of GA-RBF neural network are as follows:

1) Chromosome coding optimization. In this paper, we use the gray binary coding method to randomly convert the two optimization parameters chromosome of initial Gaussian basis function width vector σ_i and weight ω_i in RBF neural network into corresponding binary mixed coding, and carry out dissimilarity operation on the converted binary values to get new values to generate special gray binary coding, which is simple and easy to use and conforms to the principle of coding the smallest character set, and can be directly coded for the discrete variables, while only one bit changes during the coding conversion process to avoid the discontinuity problem in ordinary binary coding. The method is simple and conforms to the principle of minimum character set coding, and can directly code discrete variables, while only one bit changes during the code conversion process, avoiding the discontinuity problem in ordinary binary coding, and can reduce the redundant solution space and improve the computational efficiency of the algorithm when performing the crossover and mutation

operations. Let the number of initial population size is P, then the chromosome encoding each generation of new population is shown in equation (6).

$$a_1, a_2, a_3, \cdots, a_i, \text{ Other } i = 1, 2, 3, \cdots, P \tag{6}$$

2) Improvement of the fitness function. The genetic error parameter is chosen as the sum of the squares of the absolute values of the difference between the desired and actual outputs of the i st genetic factor corresponding to the RBF neural network, i.e., equation (7).

$$e_i = \sum_{i=1}^{p} \left| \hat{f}_{(x_i)} - f_{(x_i)} \right|^2 \tag{7}$$

where, $\hat{f}_{(x)}$ is the desired output value of the network. $f(x)$ is the actual output value of the network.

So that the i rd genetic factor fitness function in the population is the inverse of the difference between the constant and the e_i gene error parameter, when the e_i error gradually decreases, the genetic factor fitness gradually converges to a very small value, the better the chromosome obtained, by scaling the fitness value, so that the individuals adapting to the population to obtain a greater probability of selection and through the addition of a penalty function strategy to optimize the fitness value to avoid the existence of the model of the problem of overfitting That is, the fitness function obtained by improvement is shown in equation (8).

$$\begin{cases} F = \dfrac{1}{1 + c - e_i} \cdot \dfrac{1}{g(x) + 1}, c > 0; c - e_i > 0 \\ g(x) = k(C - T) \end{cases} \tag{8}$$

where c is an arbitrary constant. $g(x)$ is the penalty function. k is the penalty coefficient. C is the constraints metric. T is the constraint threshold.

c. Genetic operation optimization

Using the gambling roulette method for population P evolutionary optimization, the probability of randomly selecting its i th genetic individual in this population is shown in equation (9).

$$P_{(\alpha_i)} = \frac{F_{(i)}}{\sum_{n=1}^{P} F_{(i)}} \tag{9}$$

After the initial selection operation through the gambling roulette method, that is, the initial adaptive crossover and mutation of the parent individuals of this class began to get a new generation of offspring individuals, in which the adaptive crossover probability and mutation probability will be continuously changed with the adaptation of the offspring population, the optimization of the mutation operation introduces randomness and maintains the diversity of individuals in order to control the diversity and the balance of the local search, and obtain the initial crossover probability, mutation probability and the offspring new The relationship between crossover probability and mutation probability is shown in Eq. (10) to Eq. (11).

$$P_a = \begin{cases} P_{a_1}\left(P_{a_1} - P_{a_2}\right)\dfrac{F_{avg} - F}{F_{avg} - F_{\min}}, F \le F_{avg} \\ P_{a_1}, F > F_{avg} \end{cases} \tag{10}$$

$$P_b = \begin{cases} P_{b_1}\left(P_{b_1} - P_{b_2}\right)\dfrac{F_{avg} - F}{F_{avg} - F_{\min}}, F \le F_{avg} \\ P_{b_1}, F > F_{avg} \end{cases} \tag{11}$$

where P_a is the crossover probability. P_{a_1} is the initial crossover probability. P_{a_2} is the new crossover probability. P_b is the mutation probability. P_{b_1} is the initial mutation probability. P_{b_2} is the new mutation probability. F_{avg} is the population mean fitness. $F_{\min}$ is the population convergence minimum fitness.

The two variant offspring individuals are obtained by randomly selecting two parents in the optimally screened parent population for crossover selection and mutation selection, comparing the fitness of the variant offspring chromosomes with that of the parent chromosomes, and if the fitness of the offspring is better than that of the parent, the offspring will be programmed with the replacement of the parent into the population P to become a new population for repeated iterative evolution, and the two offspring chromosomes obtained by crossover and mutation are expressed as The two offspring chromosomes obtained through crossover and mutation are represented as equation (12).

$$\begin{cases} \dot{\alpha}_1 = \lambda\alpha_2 + (1-\lambda)\alpha_1 \\ \dot{\alpha}_2 = \lambda\alpha_1 + (1-\lambda)\alpha_2 \end{cases} \tag{12}$$

where λ is $(0,1)$ any real number.

Where each population individual can be used as an independent computing unit in the crossover and mutation process for parallel computing optimization to achieve multi-objective parallel optimization, thus shortening the search process. Through the elite retention strategy, the individual with the best fitness is retained to the next generation to maintain the evolutionary advantage of the population At the same time, this process is not subject to the limitations of random selection, and the optimal selection of individuals is obtained directly.

1) Determine the input layer structure. The coordinates of each neuron in the input layer should correspond to the number of preoperative measured biological data types in the training samples, i.e., eye axis, mean corneal curvature, and IOL A constant, totaling three parameters. If there are m training samples, a matrix X with m rows and 3 columns should be input, where any neuron is denoted by M.

2) Determine the hidden layer structure. Each neuron of the hidden layer should have the same dimension as each neuron of the input layer. If there are n hidden layer neurons, the hidden layer should consist of a matrix of n rows and 3 columns, where any neuron is denoted by C.

3) Determine the relationship between the input layer and the hidden layer. The elements of the input layer and the hidden layer are related through the activation function, and the required activation function is required to be a locally distributed non-negative nonlinear function that is radially symmetric about the center point, and the more commonly used activation function is the Gaussian function:

$$G(r) = \exp\left(-\frac{r^2}{2\sigma^2}\right) \tag{13}$$

where r denotes the Euclidean distance between any neuron M_m in the input layer and any neuron C_n in the hidden layer, i.e:

$$r_{mn} = \left\| M_m - C_n \right\| \tag{14}$$

Then the relationship between any neuron M_m in the input layer and any neuron C_n in the hidden layer is denoted as:

$$G\left(\|M_m - C_n\|\right) = \exp\left(-\frac{1}{2\sigma^2}\|M_m - C_n\|^2\right) \quad (15)$$

Each sample with the G value of each hidden layer neuron forms a matrix of m rows and n columns [23].

The width of the Gaussian function determines the range of action of this function and can be determined by the following equation:

$$\sigma = \frac{d_n}{\sqrt{2N}} \quad (16)$$

where d_n denotes the maximum Euclidean distance between hidden layer neurons and N is the number of hidden layer neurons.

4) Determine the output layer structure. Each neuron of the output layer contains only one data we need ELP, and the number of output results should be the same as the number of input samples, so it consists of a matrix with m rows and 1 column, where m is the number of samples in the input layer, and any element is denoted by Y.

5) Determine the relationship between the hidden layer and the output layer. There is a linear mapping relationship between the hidden layer and the output layer. Assuming that the coordinates of any neuron and the weight of the output result is w, each neuron in the input layer and all the neurons in the hidden layer of the G value of 1 row and n columns of the column matrix, this matrix and all the values of the linear weighted sum of the w value corresponds to the output result.

$$\sum_{k=1}^{n} G_k w_k = G_1 w_1 + G_2 w_2 + \cdots + G_k w_k \quad (17)$$

2.2.4. Training GA-RBF Neural Networks. The previously prepared training samples are organized. The training samples for the input layer are matrix X, where each row of data is organized in the order AL,K,A [24]. The ELPs corresponding to each row of matrix X form the column matrix Y, which is the training sample for the output layer. When the same crystal model is fixed, i.e., when the A constant is fixed, the overall nonlinear surface can be observed from the three-dimensional plots formed by AL, K, and ELP.

This result is saved in the form of binary data file in the disk and this completes the training of GA-RBF neural network. The flowchart of training GA-RBF neural network is shown in Fig. 2.

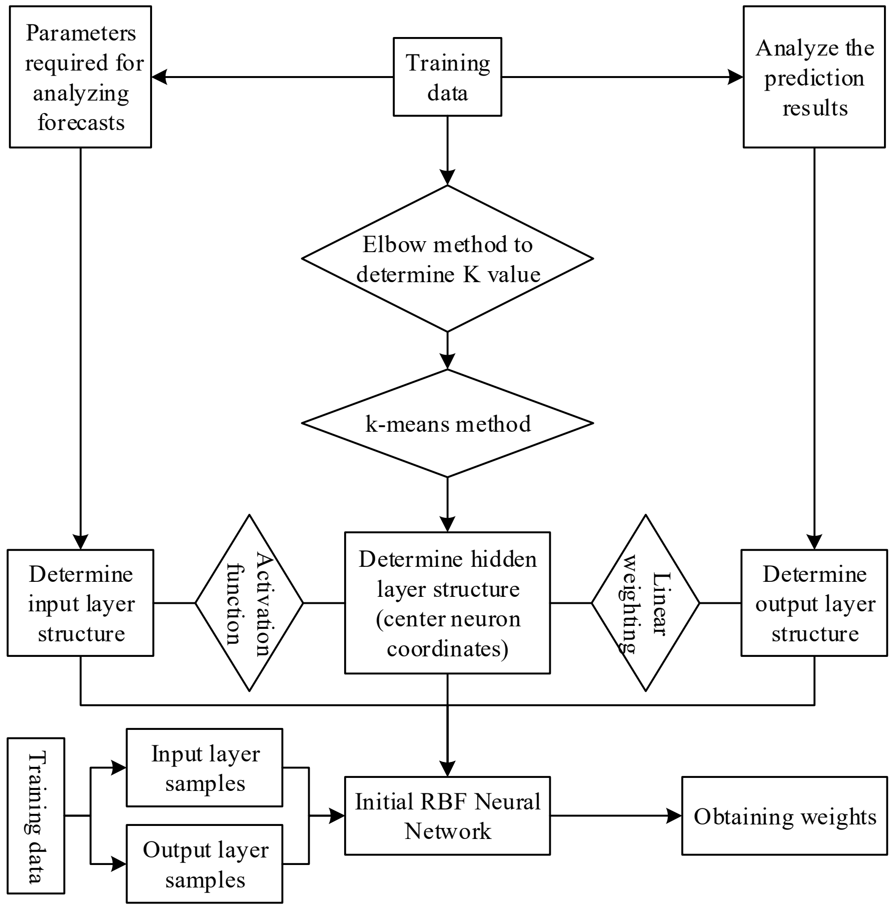

Fig. 2. Training GA-RBF neural network flow chart

2.2.5. Completion of new IOL formulae. The flowchart of the calculation principle of the GA-RBF formula is shown in Fig. 3. After obtaining AL, K, A for the new IOL formula, the trained RBF neural network was used to predict the ELP in the first step, and $AL, K, ELP, Rx = 0$ was substituted into the formula in the second step to derive the IOL refractive power $P_{emmetropia}$ that was expected to be orthoptic, and $P_{emmetropia}$ was rounded off in the third step with an accuracy of 0.5 and added with $(4.0, 3.5, 3.0, 2.5, 2.0, 1.5, 1.0, 0.5, 0.0, -0.5)$ to obtain the arrays of the refractive power of the crystals for reference, respectively, and the fourth step in turn In the fourth step, the refractive power of AL, K, ELP and the reference crystalline refractive power were substituted into the formula to invert the corresponding reserved refractive error, and in the fifth step, all the reference crystalline refractive powers and the corresponding reserved refractive errors were displayed.

At this point, we have developed a new IOL refractive power calculation formula, which we will call the GA-RBF IOL calculation formula.

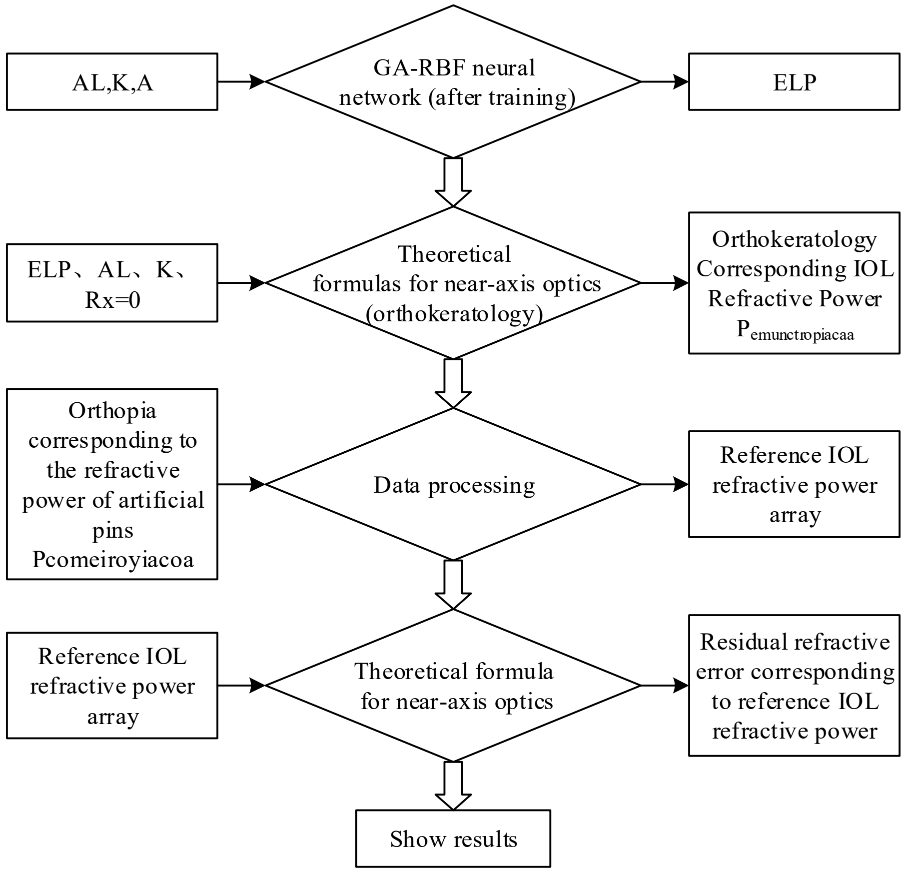

Fig. 3. The GA-RBF formula is a flowchart

3. Experiments and analysis of results

3.1. Human eye model based on cataract clinical data

3.1.1. Eye modeling. The model designed in this paper was created in optical design software, and the preoperative near-axis schematic eye model was created for three age groups, 21-40, 41-60, and 61-90 years old, respectively, consisting of the anterior and posterior surfaces of the cornea, atrial aqueous humor, lens with gradient refractive index, vitreous humor, and retina. Therefore, when the biometric data were insufficient, the parameters within the Liou-Brennan eye model were used as substitutes because the Liou-Brennan eye model was closer to the real eye configuration than the other models.

According to clinical data, the anterior chamber depth decreases and the lens thickness increases with age. In this study, the lens thickness was measured using biometric data from clinical data, while the anterior and posterior surface radii of the lens and the aspheric coefficients were substituted using parameters within the Liou-Brennan eye model. The basic parameters of the preoperative human eye model were organized to establish the preoperative model by analyzing the clinical data. The parameters of the preoperative visual acuity model are shown in Table 1.

According to the imaging characteristics of the eye, in order to more closely match the real observation effect of the human eye, the ability of the human eye to receive light of different wavelengths was weighted separately to more closely simulate the state of bright vision of the real human eye, so the wavelengths of the light were adopted as 470 nm, 510 nm, 555 nm, 610 nm and 650 nm, and the weights of the wavelengths were adjusted according to the sensitivity of the optic cells to the wavelengths as follows, respectively 0.091, 0.503, 1.000, 0.503, and 0.107.

The refractive indices of the components in the eye model were adopted from the parameter values of the Liou-Brennan eye model. In the Liou-Brennan eye model the refractive index of the cornea was 1.378, the refractive index of the aqueous humor was 1.3448, the lens used the gradient refractive index Grad A and Grad P surfaces, and the refractive index of the vitreous humor was 1.252.Since the Liou-Brennan eye model does not give explicitly the Abbe number of each refractive medium, the Abbe number was replaced by the value in the Navarro values from the eye model were substituted.

Table 1. The parameters of the preoperative eye model

Ocular parameter	Preoperative close shaft motioning eye model	Liou-brennan eye model	Navarro eye model
Anterior cornea curvature radius Rca (mm)	7.721±0.322	7.78	7.82
Anterior cornea surface cone coefficient Qca	-0.22±0.311	-0.21	-0.35
Curvature radius Rcp (mm)	Rcp=0.823xRca	6.35	6.42
The surface cone coefficient after the cornea Qcp	-0.21	-0.62	0
The central thickness of the cornea CCT (μm)	536.211±32.511	500	560
Corneal refractive index n/Vd	1.378/55.8	1.378/55.8	1.378/55.8
Water thickness ACD (mm)	3.285±0.514	3.26	3.03
Water index of room water n/Vd	1.3448/51.25	1.3448/51.25	1.3448/51.25
The curvature radius of the anterior surface of the lens Ria(mm)	12.52	12.52	10.15
The anterior surface cone coefficient of the lens Qia	-0.96	-0.96	-3.122
The curvature radius of the posterior surface of the lens Rip (mm)	-8.12	-8.12	-6.3
The surface cone coefficient of the posterior lens Qip	+0.97	+0.85	-1.1
Lens thickness LT (mm)	4.122±0.522	4.15	4
Refractive index of the lens n	Grad A/Grad P	-	-
Vitreous thickness VL (mm)	16.251	16.22	16.502
Vitreous index n / Vd	1.252/52.6	1.252/52.6	1.252/52.6
Radius of retinal curvature Rr (mm)	-11	-11	-11

3.1.2. Evaluation of visual quality. The near-axis schematic eye models of three groups (21~40 years old, 41~60 years old, and 61~90 years old) based on cataract clinical data were established according to age. The preoperative near-axis schematic eye model was initially formed and optimized by establishing the eye model, and then the image quality of the eye model was analyzed, and the commonly evaluated parameters included point-list plots, modulation transfer function MTF, and Zernike polynomials.The preoperative schematic eye model for the age of 21~40 years is shown in Fig. 4. Among them, Fig. (a) shows the three-dimensional view of the near-axis schematic eye model we built for 21~40 years old, and the refractive surfaces are the anterior surface of the cornea, the posterior surface of the cornea, the anterior surface of the lens, the virtual surface, the posterior surface of the lens, and the surface of the retina from left to right, and the model has an AL of 22.368 mm.The results of the data of the optimized data of the eye model built using the clinical data for the 21~40 years old eye model are shown in Table 2. Figure (b) shows the MTF curves for the 21- to 40-year-old eye model, with MTF values decreasing from 1 to 0.616 for the central field of view and 1 to 0.582 for the 3.5° field of view over the course of a spatial frequency of 0 lp/mm to 100 lp/mm.The MTF value decreased from 1 to 0.556 for the 5° field of view.The quality of the imaging decreased slightly with the shift in the angle of the field of view. Figure (c) is a dot-list plot of the 21- to 40-year-old eye model with an RMS radius of 2.221 μm and a GEO radius of 5.112 μm for the primary visual field angle, and an RMS radius of 4.814 μm and a GEO radius of 15.292 μm over a 5° visual field. As the field of view angle increased, a significant hysteresis was produced in the diffuse spot and the RMS and GEO radii increased. Figure (d) shows the Zernike polynomials for the 21- to 40-year-old eye model, where the translation in the low-order aberration is -2.429 × 10-3 and the defocus is 2.153 × 10-2. The spherical aberration in the higher order aberration is 1.947 × 10-2, the cloverleaf aberration is 1.62 × 10-5, and the secondary spherical aberration is -2.69 × 10-4. The defocusing aberration increases gradually as the field of view angle increases, and vertical tilt, image dispersion, tilted cloverleaf, and vertical coma are added.

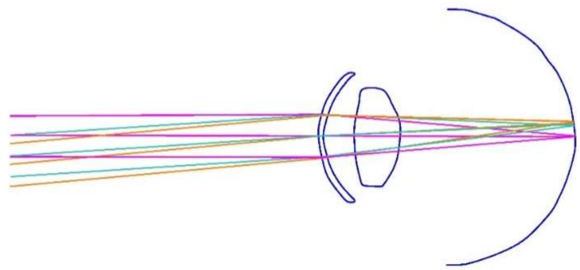

(a) The three-dimensional view of the close axial signal eye model

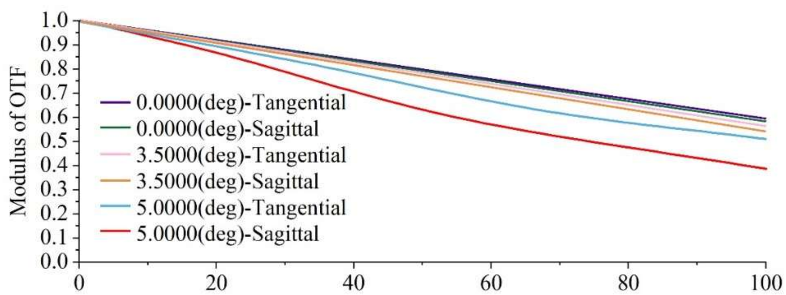

(b) MTF curve of eye model

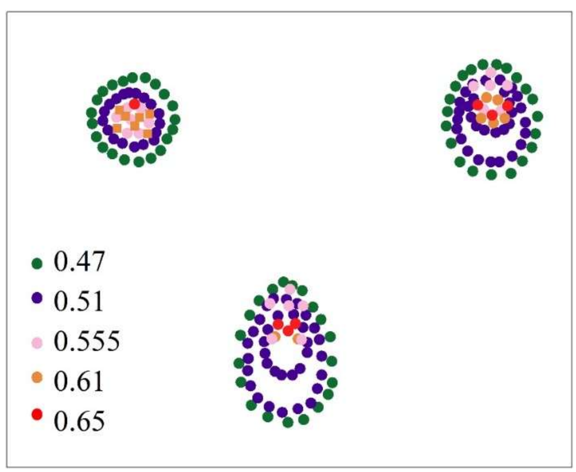

(c) The point of the eye model

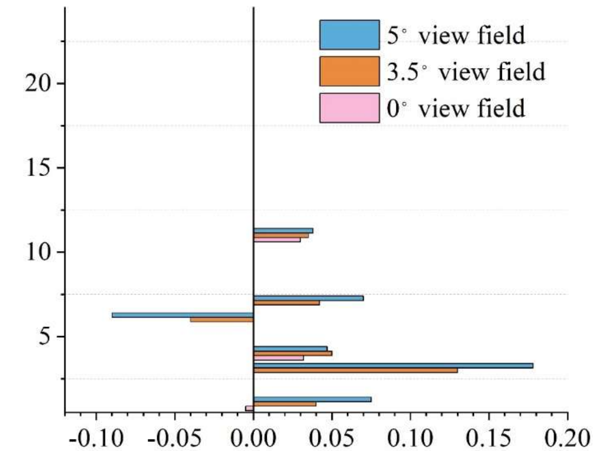

(d) Zernike polynomial

Fig. 4. The preoperative motion-eye model

Table 2. The optical parameters of the ocular model before operation

Surface	Curvature Radius	Thickness	n/Vd	Light aperture	Coefficient of non-sphere
Anterior cornea	7.795	0.488	1.266/55.84	5.895	-0.221
Posterior surface of the cornea	6.622	2.926	1.251/48.62	5.895	-0.62
Anterior surface of the lens	12.8	1.585	Grad A	4.7	-0.97
Virtual surface	Infinite	2.725	Grad P	4.7	-
Posterior surface of the lens	-8.3	17.255	1.3352/51.85	4.7	0.92
retina	-13	-	-	14	-

The comparison of the MTF curves of the eye models of the three age groups is shown in Fig. 5 (Fig. a is the global plot and Fig. b is the detail plot). As shown in Fig. (a), the MTF curve plots of the three human eye models at different ages are compared, and it can be seen that the imaging quality of the human eye decreases with age. Figure (b) is a detail of the MTF curve at 95-100 lp/mm for Figure (a).

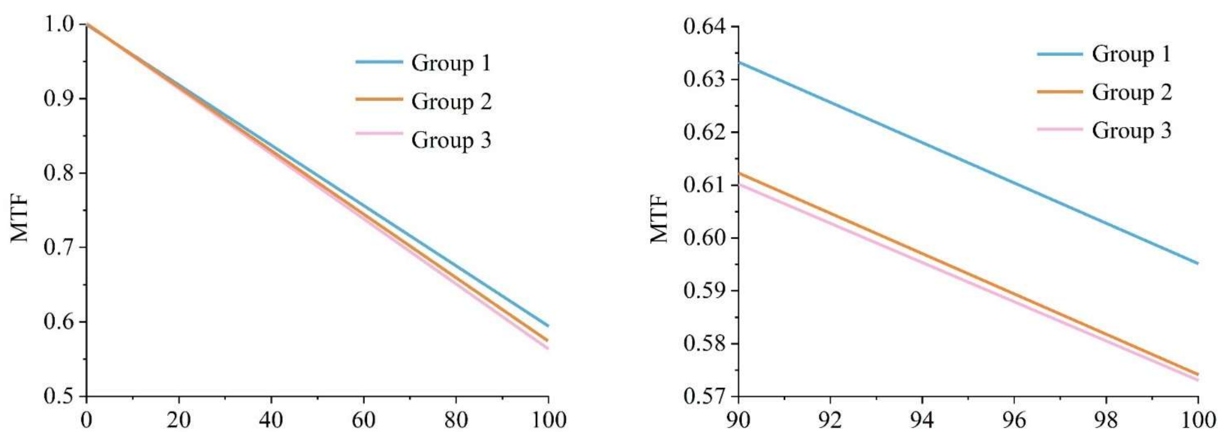

(a) Global diagram (b) Detail drawing

Fig. 5. The comparison of the MTF curve of the three age group

The eye models of 21-40, 41-60, and 61-90 years of age established on the basis of clinical data were compared and analyzed with the Liou-Brennan and Navarro eye models, and the comparison of Groups 1, 2, and 3 with the Liou-Brennan and Navarro eye models is shown in Fig. 6 (Figs. a~c are dot-column plots, Zernike polynomials, and MTFs, respectively). The RMS and GEO of the 21-40 year old eye model in Fig. (a) are better than those of the Liou-Brennan eye model, and the dispersed spot sizes of the 41-60 year old as well as the 61-90 year old eye models are slightly larger, and the dispersed spot sizes of the Navarro eye model are more different from those of the other models. The translation and defocus in the Zernike polynomials are significantly larger in the Navarro eye model than in the other eye models in Fig. (b), and the lower-order aberrations are smaller in the 21- to 40-, 41- to 60-, and 61- to 90-year-old eye models than in the Liou-Brennan eye model. Overall, the imaging quality profiles of the 21- to 40-, 41- to 60-, and 61- to 90-year-old eye models were consistent with the Liou-Brennan eye model and superior to the Navarro eye model. The resolution of the model in Fig. (c) is superior to the Liou-Brennan and Navarro eye models at 100 lp/mm. Groups 1, 2, and 3 and Liou-Brennan and Navarro.

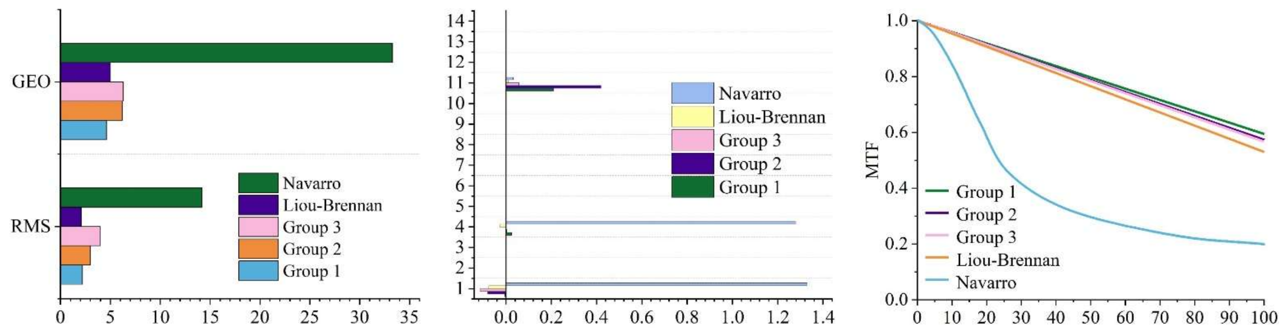

(a) Spot diagram (b) Zernike polynomial (c) MTF

Fig. 6. The 1th and 3 groups and liou-brennan and the navarro eye model are compared

By comparing the corneal refractive power, lens refractive power, and the total refractive power of the eye in the five eye models, the refractive power of the human eye models is shown in Table 3. The refractive power of the 21- to 40-year-old and 41- to 60-year-old eye models was similar to that of the Liou-Brennan eye model, whereas the larger refractive power of 62.163 for the 61- to 90-year-old eye model may be related to presbyopia or hyperopia, whereas the discrepancy in the Navarro eye model is most likely related to the fact that the data sample for this model was based on males.

Table 3. Human eye model diopter

Preoperative human eye model	Group 1	Group 2	Group 3	Liou-Brennan	Navarro
Corneal diopter	42.281	40.855	43.374	42.376	44.133
Lens dioptric	20.952	22.354	22.743	21.486	22.726
Full eye dift	60.235	60.1972	62.163	60.693	60.777

We used the clinical data of cataract patients from Xi'an People's Hospital to model the structure of the human eye. Based on the collected clinical profile data, the age-dependent parameters were anterior chamber depth, lens thickness, and vitreous length. Based on these biometric parameters, three groups (21-40, 41-60, and 61-90 years old) of near-axis schematic eye models at different age levels were designed based on Liou-Brennan, and the imaging quality of these eye models was analyzed in relation to Liou-Brennan and Navarro eye models.

Dot-list plots, MTF, and Zernike polynomials were used as criteria for assessing imaging quality. As the eye structure changed from 21 to 40 to 61 to 90 years of age, the radius of the diffuse spot grew progressively, the MTF values at a spatial frequency of 100 lp/mm decreased progressively, and the imaging quality declined with age as the values of the out-of-focus in the lower-order aberrations and the vertical astigmatism in the higher-order aberrations, the vertical wisps, the tilted second-order aberrations, and the spherical aberrations all increased progressively. In the same eye model, vertical tilt and defocus also increased as the number of visual field angles increased, and the value of vertical coma also increased, which is similar to the predictions of Bakaraju's model. Axial length and refractive power did not differ significantly between 21-40 and 41-60 years of age, and axial length and total refractive power of the eye decreased in the 61-90 year old eye model compared to the 21-40 and 41-60 year old eye models.This change in axial length may be related to age-related diseases such as myopia and presbyopia, when the 21-40 and 41-60 year old models are compared to the 61-90 year old eye model. Related. In the adult preoperative schematic eye model, the anterior chamber depth decreased and the lens thickness and axial length increased with age, and the adult preoperative schematic eye model showed similar changes in these aspects.

3.2. Experiments comparing the accuracy of the formula for calculating IOL refraction

3.2.1. Comparison of baseline data of included patients. Comparison of baseline data of the included patients is shown in Table 4 (Group A: 26 mm ⩽ AL < 27 mm. Group B: 27 mm ⩽ AL < 28 mm. Group C: 28 mm ⩽ AL < 29 mm. Group D: 29 mm ⩽ AL < 30 mm. Group E: AL ⩾ 30 mm). Preoperatively, the difference in axial length was statistically significant between the groups (p<0.05), but the differences in gender composition, age, mean corneal curvature (Km) and anterior chamber depth (ACD) were not statistically significant (p>0.05).

Table 4. Include baseline data comparison

Group	Number	Male/Female (Example)	Age($\bar{X}$ ±s,age)	AL($\bar{X}$ ±s,mm)	Km($\bar{X}$ ±s,D)	ACD($\bar{X}$ ±s,mm)
Group A	38/38	16/28	71.32±2.41	25.63±3.88	45.62±1.46	3.44±0.39
Group B	32/32	18/12	69.25±10.78	27.84±0.54	43.62±1.2	3.36±0.19
Group C	43/43	23/21	67±1.95	28.65±8.88	43.12±1.37	3.41±0.44
Group D	31/31	14/18	68.25±8.53	29.36±9.07	43.58±1.46	3.58±0.36
Group E	29/29	14/10	62.84±10.61	32.25±7.17	44.17±1.98	3.52±0.06
χ^2 / F		16	2.265	43.512	1.036	1.533
P		0.301	0.069	<0.001	0.532	0.122

3.2.2. Comparison of the accuracy of four IOL refractive error calculation formulas. Comparison of the accuracy of the four IOL refractive error formulas is shown in Table 5 (Group A: 26mm ⩽ AL < 27mm. Group B: 27mm ⩽ AL < 28mm. Group C: 28mm ⩽ AL < 29mm. Group D: 29mm ⩽ AL < 30mm. Group E: AL ⩾ 30mm). Comparison of the accuracy of the four IOL refractive error calculation formulas is shown in Fig. 7 (a, c, e, g, i are the comparison of MNE for each formula in group A~E, and b, d, f, h, j are the comparison of MAE for each formula in group A~E, respectively). The MNE and MAE of the formulas in this paper were relatively small in each group, and the MNE and MAE did not increase significantly with the growth of the eye axis, while the MAE and MNE of the SRK/T and Holladay 1 formulas increased significantly with the growth of the eye axis, and the MNE and MAE of the Holladay 1 formulas in the C, D, and E groups increased more significantly.

Table 5. The accuracy of the four artificial lens dioptometry formula was compared

Group	Formula	MNE	MAE
Group A(n=38)	Ours	0.06(-0.41,0.19)	0.22(0.27,0.51)
	SRK/T	0.31(0.01,0.34)	0.28(0.1,0.69)
	Holladay 2	-0.25(-0.65,0.27)	0.25(0.22,0.77)
	Holladay 1	-0.24(-0.39,0.23)	0.51(0.3,0.49)
Group B(n=32)	Ours	-0.2(-0.32,0.28)	0.18(0.07,0.48)

	SRK/T	0.24(-0.35,0.49)	0.12(0.09,0.59)
	Holladay 2	-0.23(-0.77,0.09)	0.67(0.34,0.8)
	Holladay 1	-0.36(-0.8,-0.06)	0.41(0.13,0.9)
Group C(n=43)	Ours	-0.24(-0.41,0.53)	0.26(0.29,0.53)
	SRK/T	-0.16(-0.73,0.2)	0.31(0.11,0.61)
	Holladay 2	-0.56(-0.61,-0.03)	0.54(0.25,0.72)
	Holladay 1	-0.54(-0.95,-0.13)	0.47(0.56,0.75)
Group D(n=31)	Ours	-0.07(-0.52,0.19)	0.36(0.03,0.85)
	SRK/T	-0.23(-0.53,0.16)	0.22(0.3,0.74)
	Holladay 2	-0.69(-1.11,0.38)	0.54(0.5,0.99)
	Holladay 1	-0.74(-1.1,-0.42)	0.75(0.44,1.11)
Group E(n=29)	Ours	-0.18(-0.34,0.2)	0.26(0.3,1.15)
	SRK/T	-0.08(-0.65,0.32)	0.36(0.22,0.69)
	Holladay 2	-0.71(-1.32,-0.62)	0.68(0.52,1.28)
	Holladay 1	-0.77(-1.12,-0.42)	0.82(0.66,1.02)

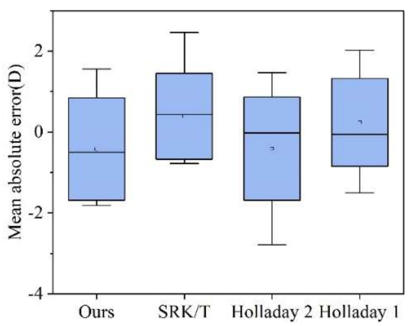

(a) A group of formula MNE comparison

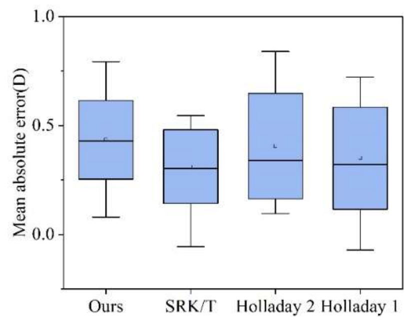

(b) A group of formula MAE comparison

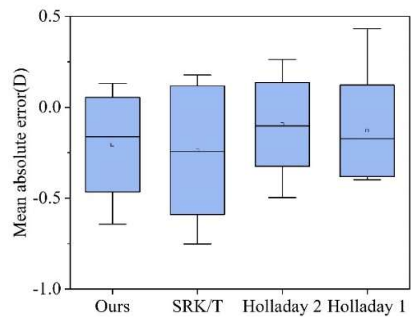

(c) B group of formula MNE comparison

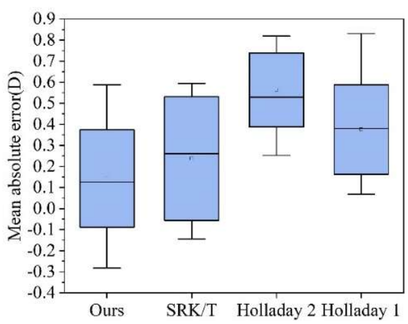

(d) B group of formula MAE comparison

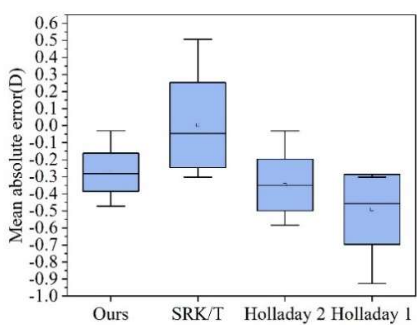

(e) C group of formula MNE comparison

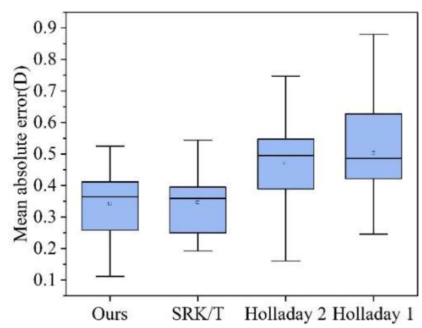

(f) C group of formula MAE comparison

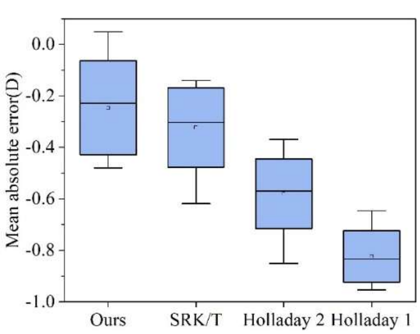

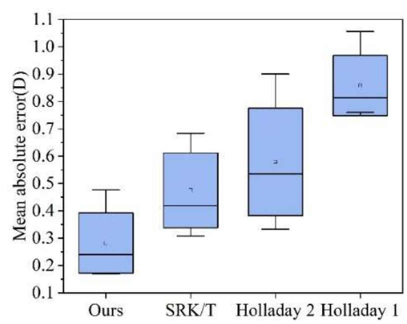

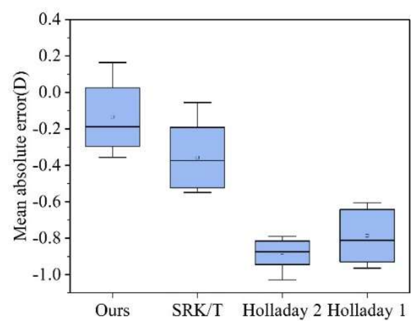

(g) D group of formula MNE comparison

(h) D group of formula MAE comparison

(i) E group of formula MNE comparison

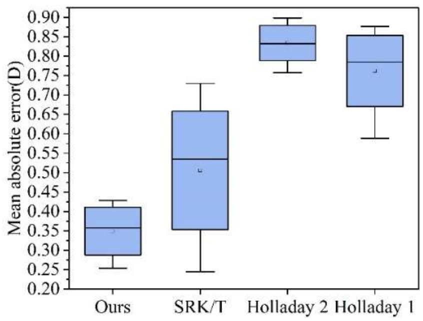

(j) E group of formula MAE comparison

Fig. 7. The accuracy of the four artificial lens dioptometry formula was compared

The distribution of the four IOL refraction formula MNE is shown in Table 6 (Group A: 26mm ⩽ AL < 27mm. Group B: 27mm ⩽ AL < 28mm. Group C: 28mm ⩽ AL < 29mm. Group D: 29mm ⩽ AL < 30mm. Group E: AL ⩾ 30mm). The percentages of MNE within ±0.5D were 65% and above for this formula, 86% and above for ±1D, and 100% for ±2D in all groups. The prediction performance of this formula was better in all groups, while the percentage of MNE within ±0.5D with eye axis growth was significantly lower in the Holladay 1 and SRK/T formulas than in this formula and the Holladay 2 formula.

Table 6. The distribution of MNE was calculated by four kinds of artificial lens refractive index

Group	Formula	±0.5 D	±1 D	D
Group A(n=38)	Ours	88	93	100
	SRK/T	60	93	100
	Holladay 2	95	99	100
	Holladay 1	70	94	100
Group B(n=32)	Ours	87	98	100
	SRK/T	55	99	100
	Holladay 2	87	96	100
	Holladay 1	67	91	100
Group C(n=43)	Ours	67	91	100
	SRK/T	62	97	100
	Holladay 2	67	87	100
	Holladay 1	27	71	100
Group D(n=31)	Ours	69	86	100
	SRK/T	58	79	100
	Holladay 2	64	94	92
	Holladay 1	23	71	100
Group E(n=29)	Ours	65	88	100
	SRK/T	55	82	100
	Holladay 2	65	80	100
	Holladay 1	31	72	100

3.3. Analysis of Improvement in Effectiveness of Remote Diagnosis and Treatment

3.3.1. Comparison of postoperative conditions between the two groups of patients. Compared with the control group (traditional diagnosis and treatment), the observation group's hospitalization time was significantly less, and the hospitalization cost was significantly lower (P<0.05), and a comparison of the postoperative conditions of patients in the two groups is shown in Table 7. The difference in postoperative morbidity was not statistically significant (P>0.05). Clinical research data indicate that cataract has an extremely high incidence, with one quarter of the population suffering from the disease. Ultrasound emulsification removal combined with IOL implantation has been shown to be one of the most effective ways of treating this disease, and when coupled with clinical care pathways, the results can be effectively enhanced. A comparative study was conducted in this hospital and it was found that the patient's hospitalization days were shortened from (6.32±1.5)d to (3.26±1.2)d, and the hospitalization cost decreased from (4825.32±366.21)yuan to (3441.62±322.65)yuan.

Table 7. The postoperative situation of the two groups was compared

Group	Postoperative vision	Average hospitalization time (d)	Average hospitalization fee (yuan)
Observation group(n=355)	0.52±0.08	3.26±1.2	3441.62±322.65
Control group(n=355)	0.49±0.2	6.32±1.5	4825.32±366.21
t / χ^2	2.0362	34.625	65.632
P	<0.05	<0.05	<0.05

3.3.2. Comparison of patients' satisfaction with therapeutic care in the two groups. Compared with the control group, the observation group had higher postoperative satisfaction, and the difference was statistically significant (P<0.05). Comparison of the survey of patients' treatment and care satisfaction between the two groups is shown in Table 8. Patient satisfaction increased from 93.62% to 98.31%. This result demonstrates the effectiveness of the remote diagnosis and treatment method.

Table 8. The comparison of nursing satisfaction in two groups was compared

Group	n	Satisfaction	Be Satisfied With	Discontent	Satisfaction Rate
Observation group	355	318	31	6	98.31
Control group	355	265	78	12	93.62
χ^2					14.28
P					<0.05

4. Conclusion

In this paper, a medical research was conducted around the optimization of parameters of cataract IOL calculation formula and its treatment effect in remote diagnosis, and the following conclusions were drawn in this paper:

In the accuracy comparison experiments of IOL calculation formula, the percentages of MNE within ±0.5D and ±1D of this paper's formula were 65% and 86% and above, and the percentages within ±2D were 100%. This indicates that the prediction performance of this paper's formula is better in all groups.

By comparing the group that implemented the method of this paper with the group that did not implement the method of this paper, the number of hospitalization days of the patients was significantly shortened and the hospitalization cost was significantly reduced, and the comparative difference was statistically significant (P<0.05). At the same time, patient treatment satisfaction was significantly increased, and the difference was statistically significant (P<0.05). It can be concluded that the remote diagnosis and treatment method based on the optimized cataract IOL calculation model can effectively shorten the hospitalization days and significantly reduce the treatment cost of these surgical patients, and can effectively improve the patient's satisfaction, and also ensure the treatment effect, which is worthy of popularization and application.

References

[1] Lam, D., Rao, S. K., Ratra, V., Liu, Y., Mitchell, P., King, J., ... & Chang, D. F. (2015). Cataract. *Nature reviews Disease primers*, 1(1), 1-15.

[2] Cicinelli, M. V., Buchan, J. C., Nicholson, M., Varadaraj, V., & Khanna, R. C. (2023). Cataracts. *The Lancet*, 401(10374), 377-389.

[3] Irawan, R. (2024). Cataract: An Article Review. *KESANS: International Journal of Health and Science*, 3(8), 312-322.

[4] Jiménez-Román, J., Prado-Larrea, C., Laneri-Pusineri, L., & Gonzalez-Salinas, R. (2018). Combined glaucoma and cataract: an overview. *Difficulties in cataract surgery*, 79-89.

[5] Mackenbrock, L. H., Labuz, G., Baur, I. D., Yildirim, T. M., Auffarth, G. U., & Khoramnia, R. (2024). Cataract Classification Systems: A Review. *Klinische Monatsblätter für Augenheilkunde*, 241(01), 75-83.

[6] Nizami, A. A., Gurnani, B., & Gulani, A. C. (2024). Cataract. *In StatPearls [Internet]*. StatPearls Publishing.

[7] Grzybowski, A., & Kanclerz, P. (2020). Recent developments in cataract surgery. *Current concepts in ophthalmology*, 55-97.

[8] Turnbull, A. M., Crawford, G. J., & Barrett, G. D. (2020). Methods for intraocular lens power calculation in cataract surgery after radial keratotomy. *Ophthalmology*, 127(1), 45-51.

[9] Zhang, J., Xia, Z., Han, X., Liu, Z., Lin, H., Qiu, X., ... & Liu, Y. (2022). Accuracy of intraocular lens calculation formulas in patients undergoing combined phakic intraocular lens removal and cataract surgery. *American Journal of Ophthalmology*, 234, 241-249.

[10] Leffler, C. T., Klebanov, A., Samara, W. A., & Grzybowski, A. (2020). The history of cataract surgery: from couching to phacoemulsification. *Annals of Translational Medicine*, 8(22).

[11] Keay, L., Lindsley, K., Tielsch, J., Katz, J., & Schein, O. (2019). Routine preoperative medical testing for cataract surgery. *Cochrane database of systematic reviews*, (1).

[12] Rossi, T., Romano, M. R., Iannetta, D., Romano, V., Gualdi, L., D'Agostino, I., & Ripandelli, G. (2021). Cataract surgery practice patterns worldwide: a survey. *BMJ open ophthalmology*, 6(1), e000464.

[13] Narayan, A., Evans, J. R., O'Brart, D., Bunce, C., Gore, D. M., & Day, A. C. (2023). Laser ‐ assisted cataract surgery versus standard ultrasound phacoemulsification cataract surgery. *Cochrane Database of Systematic Reviews*, (6).

[14] Lischke, R., Sekundo, W., Wiltfang, R., Bechmann, M., Kreutzer, T. C., Priglinger, S. G., ... & Luft, N. (2022). IOL power calculations and cataract surgery in eyes with previous small incision lenticule extraction. *Journal of Clinical Medicine*, 11(15), 4418.

[15] Ferguson, T. J., & Randleman, J. B. (2024). Cataract surgery following refractive surgery: Principles to achieve optical success and patient satisfaction. *Survey of ophthalmology*, 69(1), 140-159.

[16] Khoramnia, R., Auffarth, G., Łabuz, G., Pettit, G., & Suryakumar, R. (2022). Refractive outcomes after cataract surgery. *Diagnostics*, 12(2), 243.

[17] AlDossary, S., Martin-Khan, M. G., Bradford, N. K., & Smith, A. C. (2017). A systematic review of the methodologies used to evaluate telemedicine service initiatives in hospital facilities. *International journal of medical informatics*, 97, 171-194.

[18] Langarizadeh, M., Moghbeli, F., & Aliabadi, A. (2017). Application of ethics for providing telemedicine services and information technology. *Medical Archives*, 71(5), 351.

[19] Hajesmaeel-Gohari, S., & Bahaadinbeigy, K. (2021). The most used questionnaires for evaluating telemedicine services. *BMC medical informatics and decision making*, 21(1), 1-11.

[20] Jansen-Kosterink, S., Dekker-van Weering, M., & van Velsen, L. (2019). Patient acceptance of a telemedicine service for rehabilitation care: A focus group study. *International journal of medical informatics*, 125, 22-29.

[21] Kazutaka Kamiya,Kimiya Shimizu,Yoshihiro Kitazawa,Takashi Kojima,Tomoaki Nakamura,Kazuo Ichikawa... & Japan ICL Study Group. (2024). A Multicenter Study on Clinical Outcomes of Simultaneous Implantable Collamer Lens Removal and Phacoemulsification with Intraocular Lens Implantation in Eyes Developing Cataract. Ophthalmology and therapy.

[22] Suguru Nakagawa & Kiyoshi Ishii. (2024). Simple ab externo lens capsule removal in intraocular lens reuse and intrascleral fixation for intracapsular lens dislocation: A case report.. Medicine(49),e40840.

[23] Jiao Haihan & Jin Hui. (2024). Developing a visual prediction program for residual stress in girth butt welds using GA-RBF neural network. The International Journal of Advanced Manufacturing Technology(3-4),1615-1628.

[24] Chen Yuling, Wang Chengde, Wu Baoguo & Liu Jiancheng. (2019). Study on Site Quality Assessment of Afforestation Land Based on GA-RBF Neural Network. Nature Environment & Polution Technology(4).